39th Plasmadynamics and Lasers Conference
23 - 26 June 2008, Seattle, Washington

AIAA 2008-4226

Numerical Study of Plasma-Assisted Aerodynamic Control for Hypersonic Vehicles

Nicholas J. Bisek* and Iain D. Boyd†

University of Michigan, Ann Arbor, MI, 48109, USA

and

Jonathan Poggie‡

Air Force Research Laboratory, Wright-Patterson AFB, OH, 45433-7512, USA

Plasma actuators and various forms of volumetric energy deposition have received a good deal of research attention recently as a means of hypersonic flight control. An open question remains as to whether the required power expenditures for such devices can be achieved for practical systems. To address this issue, a numerical study is carried out for hypersonic flow over a blunt nose elliptic cone to determine the amount of energy deposition necessary for flight control. Energy deposition is simulated by means of a phenomenological dissipative heating model. Validation studies of the flow simulation code in the absence of energy deposition are presented for a Mach 8 elliptic cone flow and a Mach 14 blunt elliptic cone flow. A parametric study of the effects of energy deposition is carried out for three blunt elliptic cone configurations: a 3 m long cone at Mach 12.6 and 40 km effective altitude, a 0.6 m long cone at Mach 12.6 and 40 km altitude, and a 0.2 m long cone at Mach 14.2 and 42 km altitude. Three different volumetric energy deposition patterns are considered: a spherical pattern, a 'pancake' pattern (oblate spheroid), and a 'bean' pattern (prolate spheroid). The effects of energy deposition are seen to be relatively independent of these patterns. For the 3 m cone case, the pitching moment generated by 0.5-15 kW of energy deposition is 25-75% of that generated by a 0.1 m^2 mechanical flap at 2° deflection. For the 0.6 m cone, plasma actuators provided control authority several times greater than an equivalently scaled flap, whereas the smallest cone (0.2 m) experienced an order of magnitude increase in control authority versus its equivalently scaled flap. The effectiveness of volumetric energy deposition for flight control appears to scale strongly with a nondimensional parameter based on the freestream flow kinetic energy flux.

Nomenclature

a, b, c = the equatorial radii and the polar radius of an ellipsoid
A = surface area of grid cell
C_m = moment coefficient, $[2M_p]/[\rho_\infty {u_\infty}^2 L^2 d]$
C_p = pressure coefficient, $[2(p_w - p_\infty)]/[\rho_\infty {u_\infty}^2]$
d = maximum spanwise length
E = total energy per volume
h = enthalpy
i, j, k = computational grid indices along the axial, radial, and circumferential directions
$\mathbf{J}$ = mass diffusion flux (x, y, z directions)
L = axial surface length
M_p = moment about center of gravity
$\mathbf{n}$ = normal vector
p = pressure

*Graduate Student, Department of Aerospace Engineering, 1320 Beal Avenue, Student Member AIAA
†Professor, Department of Aerospace Engineering, 1320 Beal Avenue, Associate Fellow AIAA
‡Senior Aerospace Engineer, AFRL/RBAC. Bldg. 146 Rm. 225, 2210 Eighth St. Associate Fellow AIAA
Approved for public release, distribution unlimited, WPAFB 08-0720

$\mathbf{q}$ = heat flux (translational-rotational, and vibrational-electronic)
Q = total power input by actuator
$\tilde{Q}$ = nondimensional total power input by actuator, $Q/(\rho_\infty u_\infty^3 L^2)$
Re_x = running Reynolds number, $\rho_\infty u_\infty x/\mu_\infty$
S = source term
St = Stanton number, $q_w/[\rho_\infty u_\infty (h_0 - h_w)]$
T = temperature (translational and rotational)
T_v = temperature (vibrational and electronic)
$\mathbf{u}$ = velocity vector (u, v, w)
x, y, z = streamwise, spanwise, and transverse coordinates
ϵ = emissivity
θ = angle along circumference of the body (cylindrical coordinate system)
λ = characteristic length
μ = coefficient of viscosity
ρ = mass density
σ = Stefan-Boltzmann constant, $5.67 \times 10^{-8} W/[m^2 K^4]$
$\boldsymbol{\tau}$ = viscous stress
ϕ = inclination of the deposition to the freestream flow

Subscript
s = species
w = wall
0 = stagnation
∞ = freestream

Species
N_2 = molecular nitrogen
O_2 = molecular oxygen
NO = nitric oxide
N = atomic nitrogen
O = atomic oxygen
N_2^+ = molecular nitrogen ion
O_2^+ = molecular oxygen ion
NO^+ = nitric oxide ion
N^+ = atomic nitrogen ion
O^+ = atomic oxygen ion
e^- = free electron

I. Introduction

Aerodynamic control and drag reduction are major challenges for hypersonic vehicle designers. A good deal of research attention has recently focused on hypersonic plasma interactions and plasma flow control to explore ways of confronting these challenges.[1,2]

Minimizing drag in vehicle design leads to long thin bodies with sharp leading edges. This constrains the materials available for the vehicle's Thermal Protection System (TPS) because there is a required minimum thickness which may not be achieved for a given vehicle configuration. In addition, small defects in the production of the sharp edges can result in serious or even catastrophic problems for the TPS.[3] Blunting the leading edge reduces these drawbacks but results in a much larger wave drag.[4] Recent experimental and computational research by Shang *et al.*[5] has investigated ways of reducing drag on blunt nose bodies by means of plasma injection, while research by Kremeyer *et al.*[6] and Yan[7] focused on drag reduction and flow control using laser deposition (filamentation) ahead of conic and spherical geometries.

In addition to these design constraints, traditional control surfaces (flaps) need to be positioned away from the center of gravity to extend the maneuverability of the vehicle. The location of such flaps is limited because the bow shock surrounding the vehicle will impinge on surfaces that extend beyond the shock envelope. This results in extreme pressure and heat transfer rates at the impingement point. As such,

vehicle configurations tend to be streamlined with minimal protrusions from the fuselage. Mechanically driven flaps require clearance below the surface of the flap to provide space for the flap control arm and a strong attachment point to push from. In addition, there is a small gap in the TPS as the flap extends out to deflect the flow. This gap is difficult to protect and can cause heat related damage to the vehicle. In addition, sustained cruise and other long duration hypersonic missions also suffer from nonuniform ablation of the flap causing nonuniform control authority on the vehicle.

Plasma actuators are advantageous over mechanical controllers because they do not have moving parts, can be located either in or beneath the TPS, and are uninhibited by the bow shock. This extends the range of possible locations for the actuator and allows for multiple actuators to be powered by a central energy source. They can potentially be turned on and off very rapidly, and should have a minimal aerothermal penalty when turned off. Plasma actuators can serve multiple roles. They can be used to provide steering moments,[8,9] changes in vehicle lift,[10] control of flow separation,[11,12] and local heat load mitigation.[13]

The primary objective of this research effort is to determine whether a useful degree of flight control can be achieved with practical levels of energy deposition by investigating the effects of energy deposition on a realistic hypersonic vehicle and its surrounding flow-field. In the following, we first present validation studies of the flow code, LeMANS, using relevant experimental data available in the literature. Having successfully validated LeMANS, the code is applied to investigate plasma-based aerodynamic control. We investigate how the shape, location, and input power of deposition affect vehicle control. In addition, hot wall effects, thermodynamic models, and additional vehicle configurations are explored to help draw conclusions over different flight regimes.

II. Method

Flow-field results are obtained using Computational Fluid Dynamics (CFD) to solve the Navier-Stokes equations. The CFD computations are executed using the Michigan Aerothermodynamic Navier-Stokes (LeMANS) code which was developed at the University of Michigan.[14–17]

LeMANS is a general 2D/axisymmetric/3D, parallel, unstructured finite-volume CFD code. The numerical fluxes between cells are discretized using a modified Steger-Warming Flux Vector Splitting (FVS) scheme, except near shock waves. In these regions the original Steger-Warming FVS scheme is used.

LeMANS may be employed with any of three thermodynamic models: perfect gas, equilibrium thermochemistry, and non-equilibrium. LeMANS employs a two-temperature model to account for thermal nonequilibrium and a standard finite rate chemistry model for nonequilibrium chemistry. The two temperature model assumes that a single temperature T accounts for the translational and rotational energy modes of all species while the vibrational and electronic energy modes are accounted for by a separate temperature T_v.

The simulations are performed using second-order accurate spatial discretization and carry double precision arithmetic throughout. Thermal equilibrium and a five species finite rate air chemistry model (N_2, O_2, NO, N, and O) are used in the simulations presented unless otherwise stated.

For a single temperature (equilibrium) model with finite rate chemistry:

$$\frac{\partial \rho_s}{\partial t} + \nabla \cdot (\rho_s \mathbf{u} + \mathbf{J}_s) = \dot{\omega}_s \tag{1}$$

$$\frac{\partial \rho \mathbf{u}}{\partial t} + \nabla \cdot (\rho \mathbf{u}^2 + p\boldsymbol{\delta} - \boldsymbol{\tau}) = 0 \tag{2}$$

$$\frac{\partial E}{\partial t} + \nabla \cdot ((E+p)\mathbf{u} - \boldsymbol{\tau} \cdot \mathbf{u} - \mathbf{q} + \Sigma \mathbf{J}_s h_s) = S \tag{3}$$

For the two temperature (nonequilibrium) cases, the following vibrational energy equation is also employed.

$$\frac{\partial E_v}{\partial t} + \nabla \cdot ((E_v)\mathbf{u} - q_v + \Sigma \mathbf{J}_s e_{v,s}) = \dot{\omega}_v \tag{4}$$

LeMANS assumes the fluid is continuous and Newtonian. It assumes Stokes' hypothesis when determining the viscous stresses. The species mass diffusion flux is determined using Fick's law modified to enforce that

the sum of the diffusion fluxes is zero and plasma charge neutrality. A harmonic oscillator is used to model the species vibrational energy per unit mass ($e_{v,s}$).

For the nonequilibrium cases, we assume that 100% of the deposition energy goes initially into the translational energy equation. As the solution converges, some of the energy transfers to into the vibrational energy equation by means of the source term ($\dot{\omega}_v$). Production of vibrational energy is due to reactions in the finite rate chemistry model and energy exchange between the translational-rotational and the vibrational-electronic energy modes. Deposition of all the energy into the translational mode is a strong assumption, but is adequate for the purpose of illustrating the effects of thermal nonequilibrium.

A thermal actuator is considered as the plasma control device in this study. It is represented by a phenomenological model of dissipative heating. This model is accounted for in the Navier-Stokes equations by the addition of a source term S to the right side of energy equation (3). The shape and location of the actuator are modeled with contours of constant S having an ellipsoidal shape.[18] The strength or total power deposited into the flow uses exponential decay from the centroid of the energy deposition pattern.

$$S = \frac{Q}{\pi^{3/2}\, a \cdot b \cdot c} e^{\left(-\left(\frac{\hat{x}}{a}\right)^2 - \left(\frac{\hat{y}}{b}\right)^2 - \left(\frac{\hat{z}}{c}\right)^2\right)} \tag{5}$$

$$\begin{aligned} \hat{x} &= (x - x_0)\cos\phi - (z - z_0)\sin\phi \\ \hat{y} &= (y - y_0) \\ \hat{z} &= (x - x_0)\sin\phi + (z - z_0)\cos\phi \end{aligned} \tag{6}$$

Variables a and b are the equatorial radii (along the x and y axes) and c is the polar radius (along the z-axis for an ellipsoid with 0° inclination to the freestream). The angle ϕ is the angle between the major axis of the ellipsoid and the freestream flow. Coordinates (x_0, y_0, z_0) represent the centroid of the ellipsoid. Note that Q represents the total power deposited in the flow and $\iiint_{-\infty}^{\infty} S\, dx\, dy\, dz = Q$

III. Validation

A. 3D Sharp Elliptic Cone

Three dimensional calculations are carried out for a Mach 8 sharp elliptic cone originally studied experimentally by Kimmel *et al.*[19,20] The cone was mounted parallel to the freestream and consisted of a 2:1 aspect ratio, a half angle along the major axis of 14°, and a length $L = 1.016$ m. It was machined from stainless steel with a 40 μm nose radius and surface roughness less than 0.81 μm. The flow conditions are listed in Table 1.

Table 1. Flow conditions for the experiment of Kimmel *et al.*[19,20]

Parameter	Value	
M	7.93	
u_∞	1180.0	$^{\mathrm{m}}/_{\mathrm{s}}$
T_∞	54.6	K
T_w	303.0	K
T_0	728.0	K
p_∞	165.0	Pa
ρ_∞	0.011	$^{\mathrm{kg}}/_{\mathrm{m}^3}$
μ_∞	3.77×10^{-6}	$^{\mathrm{kg}}/_{\mathrm{m\cdot s}}$
Re_L	3.33×10^6	

A structured grid is generated because it is known to produce better results than unstructured meshes in regions near the surface of the body and through a shock.[21] One quarter of the geometry is used in the simulation because planes of symmetry exist along the major and minor axes. The 40 μm nose radius is accounted for along the tip's minor axis, resulting in an 80 μm radius along the major axis because of the elliptic geometry.

The model is aligned with the x-axis in the axial direction, the y-axis in the horizontal direction, and the z-axis in the vertical direction. A cylindrical coordinate system is also employed with $\theta = 0°$ at the top centerline of the model (z-axis) and $\theta = 90°$ at the leading edge (y-axis) as seen in Figure 1.

A gradual increase in grid spacing is used along the conic body with the smallest spacing near the tip. Radial points are algebraically spaced to increase the number of points close to the body. Grid points are equally spaced along the circumference. As a result, cell clustering occurs near the surface and the tip of the body. A grid independence study is conducted with $i \times j \times k$ grid dimensions changing from $330 \times 40 \times 30$, to $440 \times 50 \times 40$, to $550 \times 60 \times 50$. Based on comparisons of the solutions obtained on these meshes the $440 \times 50 \times 40$ grid is considered sufficiently refined and is used in the rest of the analysis. See Ref. 22 for more details.

Cross-sectional slices of the computed surface conditions are extracted to match the locations of the experimental measurements. Figure 2(a) shows the nondimensional pressure along the circumference of the body at x/L = 0.625. The pressure is relatively constant from the top centerline ($\theta = 0°$) to the shoulder ($\theta = 45°$), followed by a noticeable rise between the shoulder and the leading edge ($\theta = 90°$). Kimmel *et al.* also provided computational results from a parabolized Navier-Stokes (PNS) solver[19,20] which are included in the figures as an additional reference.

Although the cone is sharp, the formation of the boundary layer at its tip results in a noticeable rise in pressure and temperature near the stagnation point. This rise in pressure can be seen in Figure 2(b) for two different rays. The pressure quickly relaxes as the flow proceeds along the rest of the cone due to the viscous interaction. It is worth noting that the PNS solution does not capture the behavior of the flow field in the stagnation region of the cone because of the physical simplifications inherent in that method.

The high length Reynolds number (Re_L) and overall length of the model cause the flow to transition to turbulence as it proceeds along the body. LeMANS does not currently have a turbulence model implemented, so numerical results in the transitional and turbulent regions should be disregarded. Plots of the Stanton number as a function of Reynolds number are presented in Figures 3(a), 3(b) and 3(c) for $\theta = 0°$, 45°, 88°. In all three plots, the flow starts out laminar and then transitions to turbulent as it proceeds along the body. The measured data were for $Re_L = 1.7 \times 10^6$ and 6.6×10^6, whereas the case run by LeMANS has $Re_L = 3.3 \times 10^6$. Because of flow similarity, the length Reynolds number does not affect the Stanton number in the laminar region and LeMANS accurately predicts its distribution for these cases.

B. 3D Blunt Elliptic Cone

A second three dimensional validation study is performed on a Mach 14 blunt elliptic cone originally studied experimentally by Nowlan *et al.*[23] The model was mounted parallel to the freestream and had a 2:1 aspect ratio, a half angle along the major axis of 10°, and a length $L = 0.21$ m. Details of cone geometry are provided in Fig. 4. The flow conditions are listed in Table 2.

Table 2. Flow conditions for Run 15 of the Nowlan *et al.* experiment.[23]

Parameter	Value	
Mach	14.2	
u_∞	2190.	$^{\mathrm{m}}/_{\mathrm{s}}$
T_∞	59.3	K
T_w	294.0	K
T_0	211.0	K
p_∞	51.0	Pa
ρ_∞	0.003	$^{\mathrm{kg}}/_{\mathrm{m}^3}$
μ_∞	4.3×10^{-6}	$^{\mathrm{kg}}/_{\mathrm{m \cdot s}}$
Re_L	3.17×10^5	

A structured grid is generated following the same procedures and coordinate system as the sharp elliptic cone. A grid independence study is conducted with $i \times j \times k$ grid dimensions changing from $150 \times 30 \times 30$, to $300 \times 60 \times 60$, to $380 \times 80 \times 80$. The $300 \times 60 \times 60$ grid is considered sufficiently refined and is used in

the rest of the analysis. Additional details on grid convergence are available in Ref. 22.

Figure 5 shows the nondimensional pressure along the circumference of the body at two axial locations and along two rays. Following a similar trend as the sharp cone observations, the pressure is relatively constant from the top centerline to the shoulder, followed by a gradual rise between the shoulder and the leading edge. The variation in pressure distribution along the rays is more dramatic compared to the sharp cone because the blunt tip results in a strong detached bow shock and, consequently, a large stagnation region. Stanton number distributions in Fig. 6 show the profiles obtained with LeMANS follow the same general trends as those observed in the measurements.

Overpredictions observed in the nondimensional pressure and Stanton number distributions may be due to several influences not accounted for in the simulations. Nowlan *et al.* noted an uncertainty of ±7 percent in the freestream flow conditions and the very cold freestream flow conditions ($T_\infty = 59.3$ K) could have lead to condensation on the nozzle. In addition, the CAL 48-inch shock tunnel could have developed 'frozen' freestream conditions ($T_v \gg T_\infty$) as the flow accelerated through the nozzle. Nompelis *et al.* computationally demonstrated that accounting for vibrational nonequilibrium freestream conditions greatly improved agreement between computational and experiment heat transfer measurements collected in a CAL shock tunnel for their hypersonic double-cone experiment.[24] Despite the discrepancies, overall, LeMANS effectively demonstrates its capability of accurately computing three dimensional hypersonic flows.

IV. Energy Deposition

The blunt elliptic cone geometry is selected to represent a fairly realistic hypersonic vehicle, with $L = 3$ m set as the representative vehicle length. Assuming the vehicle has constant material density, its center of gravity (CG) is located 1.95 m from the tip along the x-axis (x/L = 0.65). The model is simulated in air at 40 km altitude, a freestream velocity of 4000 $^{\mathrm{m}}/_{\mathrm{s}}$, and 0° angle of attack. The complete flow conditions are provided in Table 3.

Table 3. Flow conditions for Mach 12.6 air flow at an altitude of 40 km.

Parameter	Value	
Mach	12.6	
u_∞	4000.0	$^{\mathrm{m}}/_{\mathrm{s}}$
T_∞	250.0	K
T_w	300.0	K
T_0	8300.0	K
p_∞	289.0	Pa
ρ_∞	0.004	$^{\mathrm{kg}}/_{\mathrm{m}^3}$
μ_∞	1.6×10^{-5}	$^{\mathrm{kg}}/_{\mathrm{m{\cdot}s}}$
Re_L	3.0×10^6	

A grid independence study is conducted with $i \times j \times k$ grid dimensions changing from $300 \times 60 \times 60$, to $380 \times 80 \times 80$, to $400 \times 80 \times 120$. Grid independence is achieved with the $380 \times 80 \times 80$ grid that is used in the following simulations that include energy deposition. Details on the grid convergence study are available in Ref. 22.

A. Reference Pitching Moment

A nominal reference pitching moment is found by assuming a 2° flap with a cross-sectional area of 0.2 m × 0.5 m is attached along the vehicle's top centerline as illustrated in Fig. 7. The size and location of the flap are based on illustrations of the hypersonic test vehicle shown in Ref. 25. The control authority provided by the mechanical flap is estimated computationally by incorporating the flap with the blunt elliptic cone geometry.

The flap is accounted for in the blunt elliptic cone geometry by flaring the last 0.2 m of the cone. The flair extends around the circumference of the cone and has a 2° inclination. Extending the flair around the

circumference of the body simplifies the geometry and eliminates unnecessary complexities (ie. modeling the edge of the extended flap). Since the spanwise width of the actual flap extends 0.25 m ($\theta = 18°$) from the top centerline ($\theta = 0°$), the estimated control authority provided by the flap is computed by multiplying the increased body force within that region by its moment arm (1.05 m). This results in a pitching moment ($M_{p\,\text{flap}}$) of 22.8 N-m.

B. Parametric Study

To limit the scope of the problem, three volumetric deposition shapes are selected. Namely a sphere, pancake (oblate spheroid), and bean (prolate spheroid) are employed such that a representative volume of the ellipsoidal region ($V = 4/3\pi abc$) remains constant. The values used are listed in Table 4.

Table 4. Deposition geometry parameters for Mach 12 blunt elliptic cone ($L = 3$ m).

	a	b	c
Sphere	0.007 m	0.007 m	0.007 m
Pancake	0.01852 m	0.01852 m	0.001 m
Bean	0.001852 m	0.1 m	0.001852 m

The centroid of the deposition is positioned along the top centerline ($y_0 = 0$ m) and is at least three characteristic length scales (λ) away from the surface of the body to ensure the entire deposition is deposited into the flow-field ($\iiint_{-3\lambda}^{3\lambda} S\,dx\,dy\,dz = 0.9999Q$). This distance is the minimum length from the centroid of a spherical deposition to the surface of the body as illustrated in Figure 8.

$$x_0 = x_1 + 3\lambda \cdot ||n_{x_1}|| \tag{7}$$

$$z_0 = z_1 + 3\lambda \cdot ||n_{z_1}|| \tag{8}$$

$$\phi = \tan^{-1} \left|\left| \frac{n_{x_1}}{n_{z_1}} \right|\right| \tag{9}$$

With $3\lambda = 3a$, the values of z_0 and ϕ are determined for a given x_0 by enforcing equations (7) and (8). This determines the location of $[x_1, z_1]$ and its outward unit normal vector $\mathbf{n}$. Equation (9) is used to determine ϕ so the polar radii of the ellipsoidal deposition aligns with $\mathbf{n}$. The oblate spheroid is positioned so its major axis is parallel to the freestream flow, whereas the major axis of the prolate spheroid is perpendicular to the freestream flow.

Using the Mach 5 flat plate experiment originally studied by Kimmel *et al.*[26,27] and recent MHD power generation experiments[28] for reference, realistic power input is assumed to lie in the range of 1 kW to 15 kW. The deposition is positioned near the nose of the vehicle tip to maximize the distance from the center of gravity (CG). This is done not only to increase the moment arm of the body force due to the deposition, but also because larger force changes are observed when the actuator is placed near the leading edge bow shock.[10] The three deposition shapes are studied with variation of two additional parameters: the deposition input power (Q) and the distance along the body (x/L).

The total amount of power deposited into the flow is characterized by the nondimensional total power deposition value $\tilde{Q}$.

$$\tilde{Q} = \frac{Q}{\rho_\infty u_\infty^3 L^2} \tag{10}$$

For the cases in the study $\tilde{Q} = 4.3 \times 10^{-7}$, 1.7×10^{-6}, and 6.5×10^{-6} for Q = 1 kW, 4 kW, and 15 kW respectively. This parameter provides some information on vehicle and application scaling.

The axial location of the energy deposition is apparent after investigating the pressure coefficient and Stanton number along the top centerline ($\theta = 0°$) for the three shapes in Figure 9. Although there is a slight increase in the Stanton number, it is accompanied by a noticeable rise in the pressure coefficient, particularly in the sphere and pancake depositions. This may be due to the fact that a sphere has the minimum surface

area of a spheroid, and consequently, has the highest power deposited per projected surface area onto the body. The total force acting on the body in the Cartesian coordinate system is found by taking the scalar product of the combined stress tensor and pressure matrices with the corresponding area vector.

With the local force known, the pitching moment is determined in the conventional manner. Because of the deposition on the top half of the vehicle, the pitching moment for each scenario is its deviation from the baseline ($M_p = M_{p\,\text{deposition}} - M_{p\,\text{baseline}}$). It is normalized by the moment due to the mechanical flap ($M_{p\,\text{flap}} = 22.8$ N-m). Figure 10 plots the normalized change in pitching moment for each of the shapes. The points are fitted with a parametric spline because of their assumed non-linearity.

All simulations are computed assuming thermal equilibrium and use a 5 species finite rate chemistry model (N_2, O_2, NO, N, and O) except for the largest deposition scenario (Q = 50 kW, x/L = 0.10, 'pancake'). This scenario is repeated for two additional conditions: thermal equilibrium, 11 species chemistry model; and thermal nonequilibrium, 11 species chemistry model. The 11 species chemistry model (N_2, O_2, NO, N, O, N_2^+, O_2^+, NO^+, N^+, O^+, e) accounts for weakly ionized plasmas. These additional cases are compared against their respective baseline cases to determine the effectiveness of the deposition.

For thermal equilibrium air, the inclusion of a larger chemistry model has a relatively small impact on the total pitching moment as seen in the Q=50 kW case (equilibrium, 5 sp vs. equilibrium, 11 sp). Thermal nonequilibrium noticeably reduces the effectiveness of the energy deposition because only the energy going into the translational temperature can affect the local pressure and thus the net force. Comparing the results for the thermal equilibrium, 5 species simulations to the thermal nonequilibrium, 11 species simulations for the Q=30, 50 kW cases, it is clear that thermal nonequilibrium and weakly ionized plasma effects become increasing significant as the total power deposited increases and the flow deviates from a perfect gas.

Figure 10 shows energy deposition is able to provide the same order of magnitude of control authority as the mechanical flap. In addition, while the shape of the deposition appears to have noticeable effects on the local pressure coefficient and Stanton number, it does not appear to have a large impact on the overall change in the pitching moment (control authority).

C. Hot Wall Effect

The previous simulations used a constant wall temperature of 300 K as seen Table 3. This is cooler than the expected wall temperature of a real hypersonic vehicle. Assuming blackbody emissivity ($\epsilon = 1$), the Stefan-Boltzmann Law is used along with the computed heat flux on the body to estimate the expected wall temperature.

$$T_w = \left(\frac{q_w}{\epsilon\sigma}\right)^{1/4} \tag{11}$$

This estimated wall temperature varies from 600 - 1900 K along the cone, with an average temperature of 1000 K in the region where the deposition would be located. A new set of simulations is carried out with $T_w = 1000$ K, and all other conditions equal to those listed in Table 3. The simulations are performed using the 'pancake' deposition parameters listed in Table 4 and the centroid of the deposition located at x/L = 0.1. The moment coefficient is calculated for each simulation using equation (12).

$$C_m = \frac{M_p}{\frac{1}{2}\rho_\infty {u_\infty}^2 L^2 d} \tag{12}$$

The reference area is taken to be the maximum spanwise width ($d = 1.644$ m) multiplied by the body length ($L = 3$ m). Figure 11 plots the moment coefficient versus power deposited for two constant wall temperatures. The higher wall temperature reduces the moment coefficient (control authority) of the vehicle because a smaller portion of the energy deposited goes into the translational temperature.

V. Additional Vehicle Configurations

The freestream conditions used in the simulations of the 3 m configuration (Table 3) are also applied to two additional, scaled geometries. The 'medium' scaled vehicle has a length $L = 0.62$ m. The nondimensional total power deposition value $\tilde{Q}$ for the cases run is, $\tilde{Q} = 4.0 \times 10^{-5}$, 1.0×10^{-4}, and 1.5×10^{-4} for Q = 4 kW, 10 kW, and 15 kW respectively.

The deposition is modeled as an oblate spheroid (pancake), scaled to match the one used in the $L = 3$ m parametric study. Table 5 lists the values used to represent the energy deposition volume with the deposition positioned near the bow shock (x/L = 0.10).

Table 5. The location of energy deposition for Mach 12.6 blunt elliptic cone ($L = 0.6$ m).

a	b	c
0.00386 m	0.00386 m	0.00021 m

The moment coefficient for the simulations is found using Eq. (12) with $d = 0.343$ m. The pitching moment due to the mechanical flap is found following the approach covered in section IV.A with the large geometry flap dimensions proportionately scaled (10.5 cm × 4.2 cm). This results in a pitching moment ($M_{p\,\text{flap}}$) of 0.148 N-m. The smaller geometry produces a weaker bow shock and consequently a lower post shock temperature. Similar to section IV.C, the cooler temperature improves the control authority provided by energy deposition. However, a large spike in the Stanton number distribution is observed in Figure 12. This coincides with location of the deposition and partially recovers to the baseline distribution as the flow progresses along the body. The distribution can not fully recover because of the additional energy added to the flow.

The effects of energy deposition are also simulated for several cases using a 'small' $L = 0.21$ m blunt elliptic cone with freestream conditions found in Table 2. These conditions represent an altitude of 42 km in air, based on the unit Reynolds number. The decrease in freestream velocity along with the significantly smaller geometry increases the nondimensional total power deposition value $\tilde{Q}$ by several orders of magnitude. For the cases run, $\tilde{Q} = 4.0 \times 10^{-4}$, 8.0×10^{-4}, and 1.6×10^{-3} for Q = 500 W, 1 kW, and 2 kW respectively.

The deposition is modeled as an oblate spheroid (pancake), similar to the one used in the $L = 3$ m parametric study. Table 6 lists the values used to represent the energy deposition volume and centroid. Unlike the medium cone, the deposition shape is larger than a pro

Table 6. The location of energy deposition for Mach 14 blunt elliptic cone ($L = 0.2$ m).

x_0	y_0	z_0	a	b	c	θ
0.0292 m	0 m	0.017 m	0.003 m	0.004 m	0.001 m	0°

Compared to the previous configurations, the small geometry produces an even weaker bow shock, which further reduces the post shock temperature. In addition, the freestream temperature and total enthalpy are much lower in these simulations (refer to Table 2). This allows for a larger portion of the deposition to increase the translational temperature (net force increase). In addition, the shorter body length (L) means the flow passes over the vehicle quicker so the large temperature rise observed within the region of the deposition extends farther along the vehicle. This is apparent in the significant downstream temperatures observed in Figure 13.

Coinciding with the high temperature, a strong heat transfer penalty is detected, along with a dramatically increase in the pressure coefficient distribution (Fig. 14). Although the Stanton number remains significantly elevated downstream of the deposition, the pressure coefficient quickly returns to the baseline (equilibrium) state which is consistent to the observations seen in the large and medium cone simulations.

The moment coefficient is found using equation (12) with $d = 0.114$ m. Consistent with previous simulations, the pitching moment due to the mechanical flap is computed following the method presented in section IV.A with the large geometry flap dimensions scaled down proportionately (3.5 cm × 1.4 cm). This results in a pitching moment ($M_{p\,\text{flap}}$) of 10^{-3} N-m.

These results, along with those obtained for the medium and large blunt elliptic cone simulations, are plotted together in Figure 15 using the nondimensional total power deposition parameter $\tilde{Q}$. Figure 15(a) shows a strong correlation between $\tilde{Q}$ and the moment coefficient for the various simulations. As previously noted, the scale deposition shape of the small cone does not exactly match the medium or large cones, but these results further demonstrate the minimal contribution deposition shape has on the net control authority. The results appear to follow a near linear curve when plotted on a log-log scale ($C_m \approx \tilde{Q}^{1.1}$). The different

deposition locations, along with different vehicle lengths and freestream conditions, and real gas effects cause the results to deviate slightly from the linear curve.

Using the reference pitching moment found for each of the configurations, the normalized pitching moment for each configurations is plotted in Fig. 15(b). Again, the results follow a near linear curve on a log-log scale ($M_p/M_{p\,\text{flap}} \approx \tilde{Q}^{1.3}$) with deviations from the curve due to the aforementioned reasons. The figure shows that energy deposition is a viable replacement for a mechanical flap when $\tilde{Q} \geq 10^{-5}$. Given that $\tilde{Q} = Q/\rho_\infty u_\infty^3 L^2$, this suggests smaller geometries, flying a lower velocities, and/or higher altitudes (lower densities) would make energy deposition a viable replacement for a mechanical flap. For completeness, the pitching moment (M_p) for all simulations is listed in the Appendix Tables 7 - 10.

VI. Conclusions

The Michigan Aerothermodynamic Navier-Stokes code was successfully validated for hypersonic flow around three-dimensional blunt and sharp elliptic cones. In addition, a phenomenological heating model was implemented to investigate whether a practical level of control could be achieved from volumetric energy deposition for a realistic hypersonic vehicle. A parametric study was completed investigating the shape, location, and total amount of energy volumetrically deposited into the flow-field for two blunt-nosed elliptic cone configurations. The shape of the deposition resulted in relatively small changes in the effectiveness of the deposition, whereas an increased wall temperature noticeably decreased the moment coefficient. Thermal nonequilibrium and weakly ionized plasma effects also decrease the control authority as input power increases. The effectiveness of volumetric energy deposition for flight control appeared to scale strongly with the nondimensional parameter based on the freestream flow kinetic energy flux. It appears to be a viable means of control for configurations at higher altitude, with slower velocities, and smaller vehicle length.

Acknowledgments

The authors are indebted to the Michigan/AFRL/Boeing Collaborative Center in Aeronautical Sciences which provides funding to the first author. The first author would like to thank Leonardo Scalabrin for numerous discussions about LeMANS and Roger Kimmel for his valuable discussions on the subject. The generous use of the University of Michigan's Center for Advanced Computing and the Aeronautical Systems Center Major Shared Resource Center (ASC MSRC) were indispensable to this investigation, and are greatly appreciated.

References

[1]Fomin, V. M., Tretyakov, P. K., and Taran, J.-P., "Flow Control using Various Plasma and Aerodynamic Approaches," *Aerospace Science and Technology*, Vol. 8, No. 5, 2004, pp. 411–421.

[2]Shang, J. S., Surzhikov, S. T., Kimmel, R., Gaitonde, D., Menart, J., and Hayes, J., "Mechanisms of Plasma Actuators for Hypersonic Flow Control," *Progress in Aerospace Sciences*, Vol. 41, No. 8, 2005, pp. 642–668.

[3]Mason, W. H. and Lee, J., "Aerodynamically Blunt and Sharp Bodies," *10th AIAA Applied Aerodynamics Conference*, AIAA Paper 1992-2727, 1992.

[4]Santos, W. F. N. and Lewis, M. J., "Aerothermodynamic Performance Analysis of Hypersonic Flow on Power Law Leading Edges," *Journal of Spacecraft and Rockets*, Vol. 42, No. 4, 2005, pp. 588–597.

[5]Shang, J. S., Hayes, J., and Menart, J., "Hypersonic Flow over a Blunt Body with Plasma Injection," *Journal of Spacecraft and Rockets*, Vol. 39, No. 3, 2002, pp. 367–375.

[6]Kremeyer, K., Sebastian, K., and Shu, C.-W., "Computational Study of Shock Mitigation and Drag Reduction by Pulsed Energy Lines," *AIAA Journal*, Vol. 44, No. 8, 2006, pp. 1720–1731.

[7]Yan, H. and Gaitonde, D., "Control of Edney IV Interaction by Energy Pulse," *44th AIAA Aerospace Sciences Meeting and Exhibit*, AIAA Paper 2006-562, 2006.

[8]Girgis, I. G., Shneider, M. N., Macheret, S. O., Brown, G. L., and Miles, R. B., "Creation of Steering Moments in Supersonic Flow by Off-Axis Plasma Heat Addition," *40th AIAA Aerospace Sciences Meeting and Exhibit*, 2002, AIAA Paper 2002-129.

[9]Gnemmi, P., Charon, R., Dupéroux, J.-P., and George, A., "Feasibility Study for Steering a Supersonic Projectile by a Plasma Actuator," *AIAA Journal*, Vol. 46, No. 6, 2008, pp. 1308–1317.

[10]Menart, J., Stanfield, S., Shang, J., Kimmel, R., and Hayes, J., "Study of Plasma Electrode Arrangements for Optimum Lift in a Mach 5 Flow," *44th AIAA Aerospace Sciences Meeting and Exhibit*, 2006, AIAA Paper 2006-1172.

[11]Updike, G. A., Shang, J. S., and Gaitonde, D. V., "Hypersonic Separated Flow Control Using Magneto-Aerodynamic Interaction," *43th AIAA Aerospace Sciences Meeting and Exhibit*, AIAA Paper 2005-164, 2005.

[12]Kimmel, R. L., Hayes, J. R., Crafton., J. W., Fonov, S. D., Menart, J., and Shang, J., "Surface Discharge for High-Speed Boundary Layer Control," *44th AIAA Aerospace Sciences Meeting and Exhibit*, AIAA Paper 2006-710, 2006.

[13]Miles, R. B., Macheret, S. O., Shneider, M. N., Steeves, C., Murray, R. C., Smith, T., and Zaidi, S. H., "Plasma-Enhanced Hypersonic Performance Enabled by MHD Power Extraction," *43th AIAA Aerospace Sciences Meeting and Exhibit*, AIAA Paper 2005-561, 2005.

[14]Scalabrin, L. C. and Boyd, I. D., "Development of an Unstructured Navier-Stokes Solver For Hypersonic Nonequilibrium Aerothermodynamics," *38th AIAA Thermophysics Conference*, AIAA Paper 2005-5203, 2005.

[15]Scalabrin, L. C. and Boyd, I. D., "Numerical Simulation of Weakly Ionized Hypersonic Flow for Reentry Configurations," *9th AIAA/ASME Joint Thermophysics and Heat Transfer Conference*, AIAA Paper 2006-3773, 2006.

[16]Scalabrin, L. C. and Boyd, I. D., "Numerical Simulation of the FIRE-II Convective and Radiative Heating Rates," *39th AIAA Thermophysics Conference*, AIAA Paper 2007-4044, 2007.

[17]Scalabrin, L. C., "Numerical Simulation of Weakly Ionized Hypersonic Flow Over Reentry Capsules," Ph.D. Thesis, Univ. of Michigan, 2007.

[18]Poggie, J., "Plasma-Based Hypersonic Flow Control," *37th AIAA Plasmadynamics and Lasers Conference*, AIAA Paper 2006-3567, 2006.

[19]Kimmel, R. L., Poggie, J., and Schwoerke, S. N., "Laminar-Turbulent Transition in a Mach 8 Elliptic Cone Flow," *AIAA Journal*, Vol. 37, No. 9, 1999, pp. 1080–1087.

[20]Kimmel, R., Klein, M., and Schwoerke, S., "Three-Dimensional Hypersonic Laminar Boundary-Layer Computations for Transition Experiment Design," *AIAA Journal*, Vol. 34, No. 4, 1997, pp. 409–415.

[21]Candler, G., "Unstructured Grid Approaches for Accurate Aeroheating Simulations," *18th AIAA Computational Fluid Dynamics Conference*, AIAA Paper 2007-3959, 2007.

[22]Bisek, N. J., Boyd, I. D., and Poggie, J., "Numerical Study of Energy Deposition Requirements for Aerodynamic Control of Hypersonic Vehicles," *46nd AIAA Aerospace Sciences Meeting and Exhibit*, AIAA Paper 2008-1109, 2008.

[23]Nowlan, D., Burke, A., and Bird, K., "Pressure and Heat Transfer Distribution on ASD Elliptic Cone (W3) and ASD Sortie (W4) in the CAL 48-Inch Hypersonic Shock Tunnel," Tech. Rep. AM-1800-Y-2, Cornell Aeronautical Laboratory, Inc., Buffalo, NY, December 1963, ASC 94 2649.

[24]Nompelis, I., Candler, G., and Holden, M., "Effect of Vibrational Nonequilibrium on Hypersonic Double-Cone Experiments," *AIAA Journal*, Vol. 41, No. 11, 2003, pp. 2162–2169.

[25]Walker, S. H. and Rodgers, F., "Falcon Hypersonic Technology Overview," *13th AIAA/CIRA International Space Planes and Hypersonics Systems and Technologies Conference*, AIAA Paper 2005-3253, 2005.

[26]Kimmel, R. L., Hayes, J. R., Menart, J. A., and Shang, J., "Effect of Surface Plasma Discharges on Boundary Layers at Mach 5," *42nd AIAA Aerospace Sciences Meeting and Exhibit*, AIAA Paper 2004-509, 2004.

[27]Kimmel, R., Hayes, J., Menart, J., and Shang, J., "Supersonic Plasma Flow Control Experiments," Tech. Rep. ARFL-VA-WP-TR-2006-3006, U.S. Air Force Research Laboratory, Wright-Patterson AFB, OH, December 2005, AFRL/WS 06-0097.

[28]Velocci, A. L. J., "A General Atomics-led Team," *Aviation Week and Space Technology*, 2007.

Appendix

Table 7. Pitching moment for large cone simulations with freestream conditions found in Table 3 and deposition parameters listed in Table 4. ($L = 3$ m, $T_w = 300$ K).

Shape	x/L	Q [kW]	M_p [N-m]
thermal equilibrium, 5 sp.			
flap			22.8
sphere	0.05	1	3.73
sphere	0.05	4	5.55
sphere	0.05	15	16.81
sphere	0.10	1	4.03
sphere	0.10	4	6.91
sphere	0.10	15	16.04
bean	0.05	1	6.16
bean	0.05	4	8.86
bean	0.05	15	17.41
bean	0.10	1	5.86
bean	0.10	4	6.57
bean	0.10	15	16.97
pancake	0.05	1	3.75
pancake	0.05	4	6.54
pancake	0.05	15	17.05
pancake	0.10	1	4.35
pancake	0.10	4	6.66
pancake	0.10	15	15.51
pancake	0.10	30	18.36
pancake	0.10	50	27.28
thermal equilibrium, 11 sp.			
pancake	0.10	50	25.76
thermal nonequilibrium, 11 sp.			
pancake	0.10	30	15.9
pancake	0.10	50	21.29

Table 8. Pitching moment for large cone simulations with freestream conditions found in Table 3 and deposition parameters listed in Table 4. ($L = 3$ m, $T_w = 1000$ K).

Shape	x/L	Q [kW]	M_p [N-m]
thermal equilibrium, 5 sp.			
flap			21.6
pancake	0.10	0.5	0.58
pancake	0.10	1	0.75
pancake	0.10	4	3.22
pancake	0.10	15	10.04

Table 9. Pitching moment for medium cone simulations with freestream conditions found in Table 3 and deposition parameters listed in Table 5. ($L = 0.6$ m, $T_w = 300$ K).

Shape	x/L	Q [kW]	M_p [N-m]
thermal equilibrium, 5 sp.			
flap			0.15
pancake	0.10	4	0.36
pancake	0.10	10	0.78
pancake	0.10	15	1.08

Table 10. Pitching moment for small cone simulations with freestream conditions found in Table 2 and deposition parameters listed in Table 6. ($L = 0.2$ m, $T_w = 294$ K).

Shape	x/L	Q [kW]	M_p [N-m]
thermal equilibrium, 5 sp.			
flap			0.001
pancake	0.10	0.5	0.023
pancake	0.10	1	0.039
pancake	0.10	2	0.061

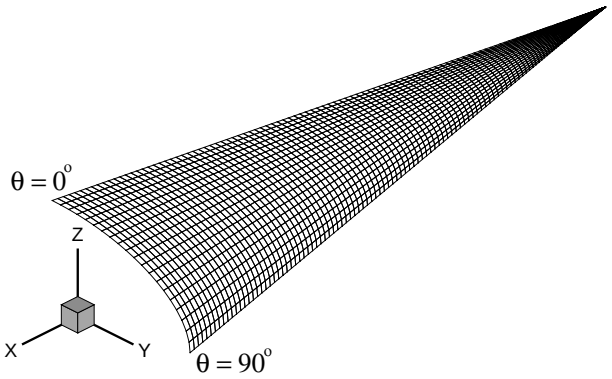

Figure 1. Surface of the sharp elliptic cone grid with both Cartesian and cylindrical coordinate systems.

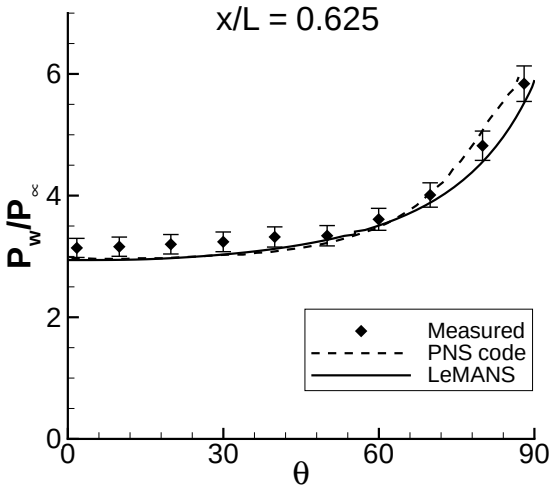

(a) Pressure around the circumference

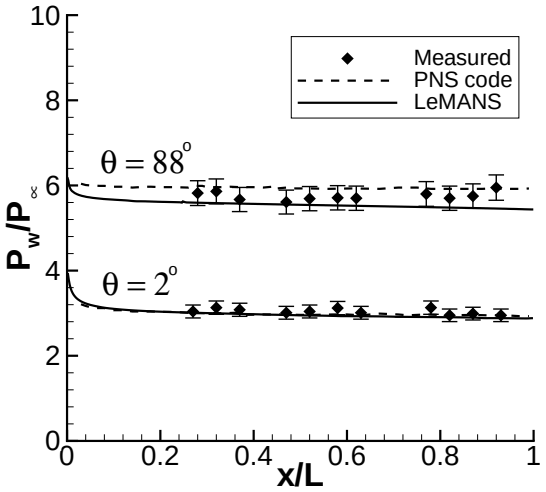

(b) Pressure along rays

Figure 2. Normalized surface pressure distributions for the Mach 8 sharp elliptic cone (±5 percent experimental uncertainty). PNS calculations and experimental data from Ref. 19.

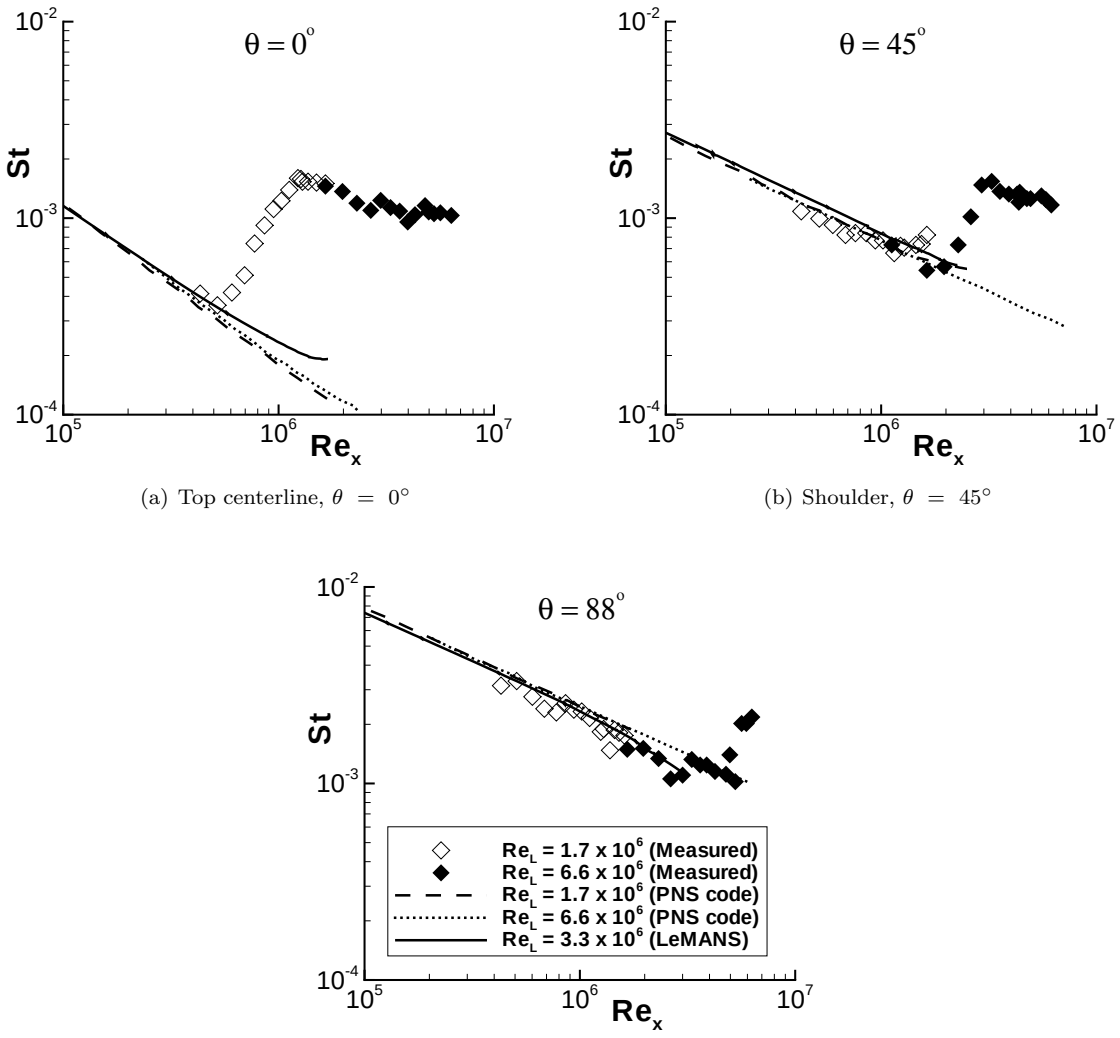

(a) Top centerline, $\theta = 0°$

(b) Shoulder, $\theta = 45°$

(c) Leading edge, $\theta = 88°$

Figure 3. Stanton number distributions for the Mach 8 sharp elliptic cone (symbol size reflects ±10 percent experimental uncertainty). Experimental data and PNS calculations from Ref. 19.

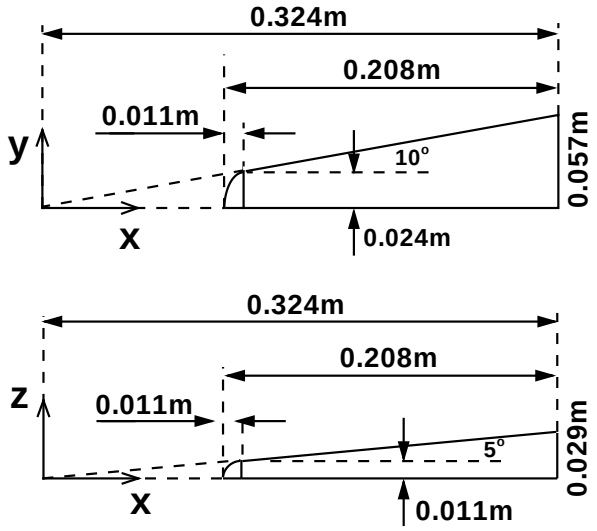

Figure 4. Blunt elliptic cone geometry. Adapted from Ref. 23.

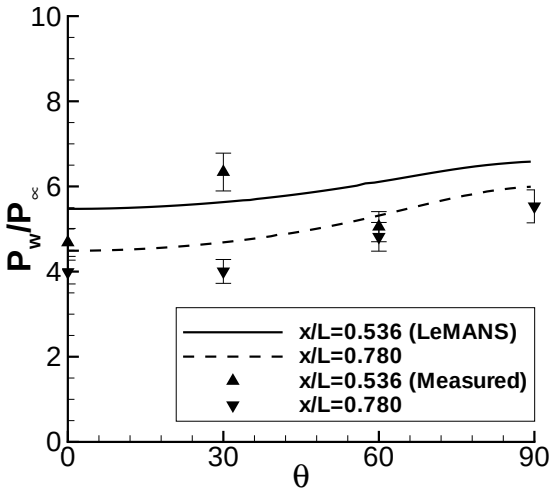

(a) Pressure around the circumference

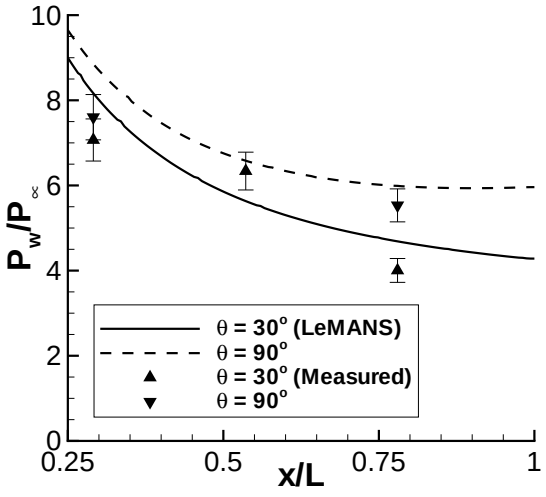

(b) Pressure along rays

Figure 5. Normalized surface pressure distributions for Mach 14 blunt elliptic cone (±7 percent experimental uncertainty). Experimental data from Ref. 23.

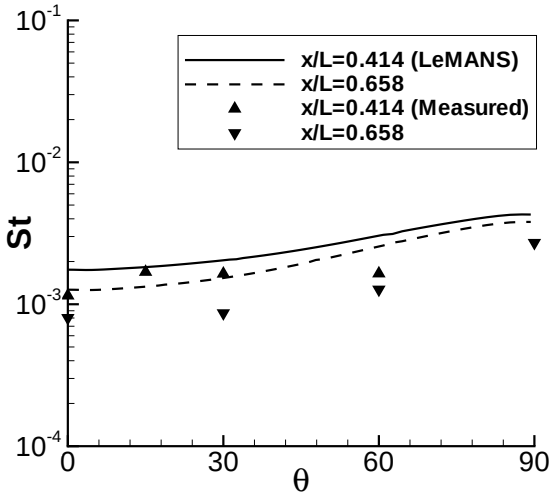

(a) Stanton number around the circumference

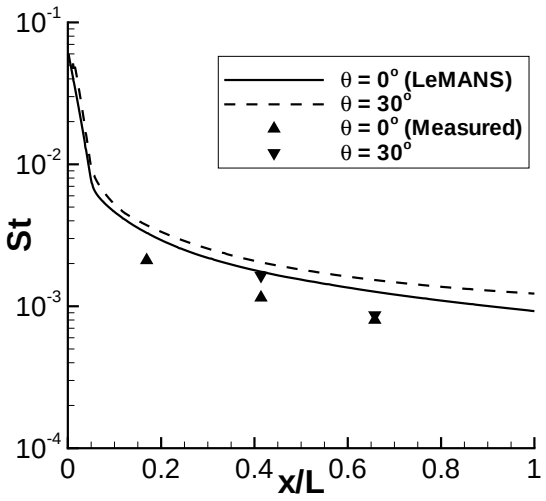

(b) Stanton number along rays

Figure 6. Stanton number distributions for Mach 14 blunt elliptic cone (symbol size reflects ±4.5 percent experimental uncertainty). Experimental data from Ref. 23.

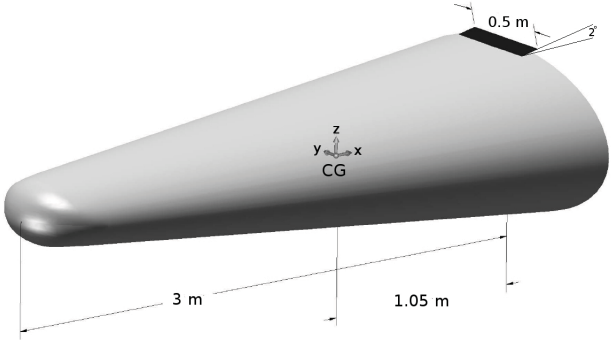

Figure 7. Model of a 2° mechanical flap attached to a blunt elliptic body.

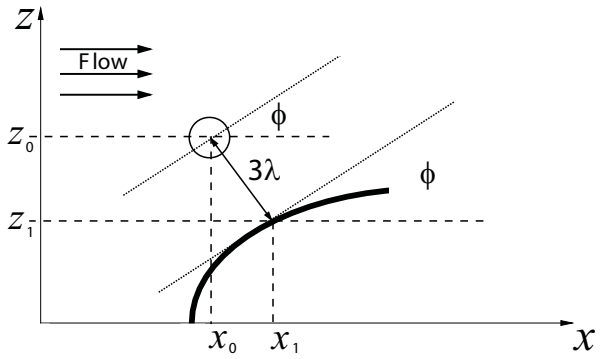

Figure 8. The constant height parameter used to determine z_0 and ϕ.

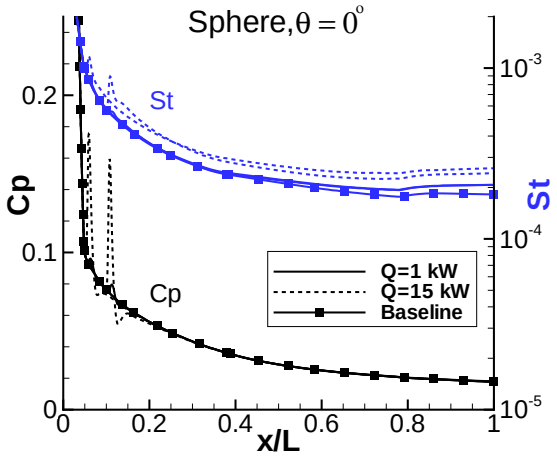

(a) Sphere deposition

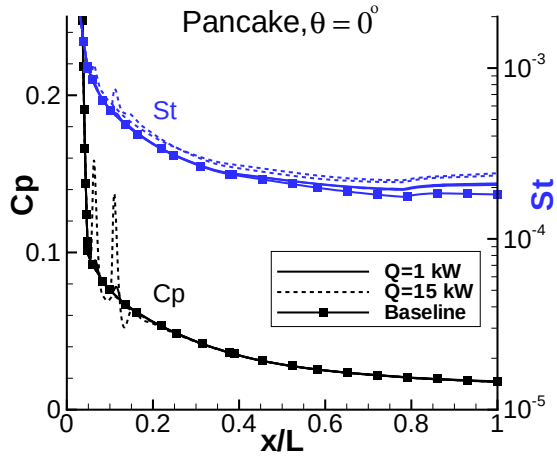

(b) 'Pancake' deposition

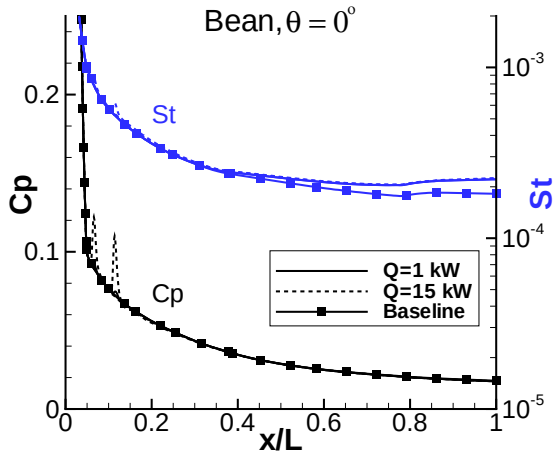

(c) 'Bean' deposition

Figure 9. Pressure coefficient and Stanton number distributions for the Mach 12 blunt elliptic cone ($L = 3$ m) for various energy deposition patterns along the top centerline ($T_w = 300$ K).

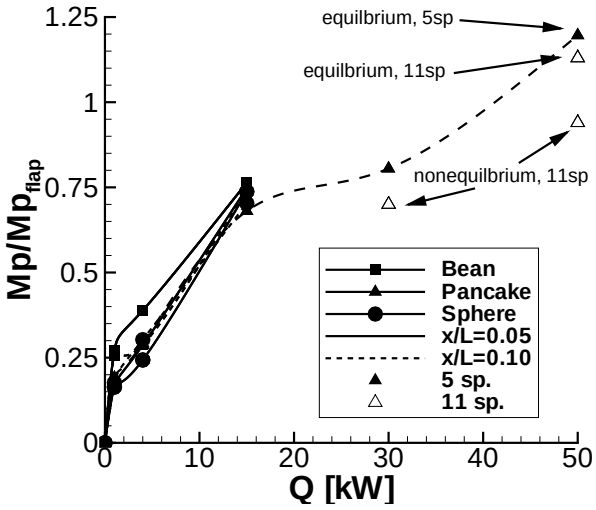

Figure 10. Normalized change in pitching moment for a Mach 12 blunt elliptic cone ($L = 3$ m) for various energy deposition patterns ($T_w = 300$ K).

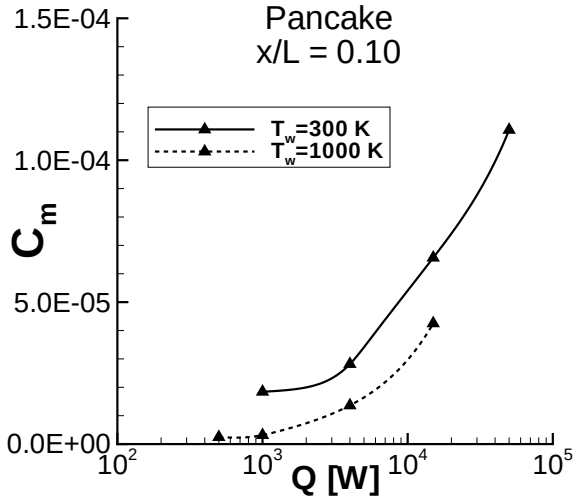

Figure 11. Moment coefficient for a Mach 12 blunt elliptic cone ($L = 3$ m) for two constant wall temperatures.

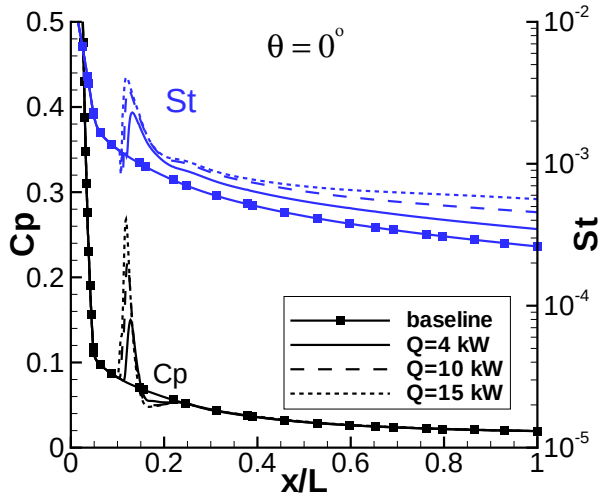

Figure 12. Pressure coefficient and Stanton number distributions along the top center line ($\theta = 0°$) of a Mach 12 blunt elliptic cone ($L = 0.6$ m) with different amounts of energy deposition ($T_w = 300$ K).

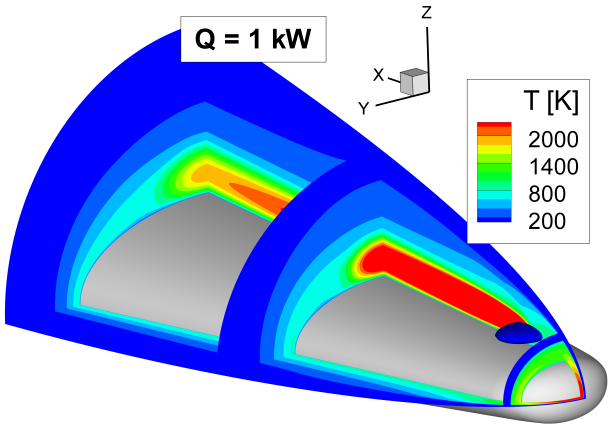

Figure 13. Temperature contours for Mach 14 blunt elliptic cone ($L = 0.2$ m) with $Q = 1$ kW.

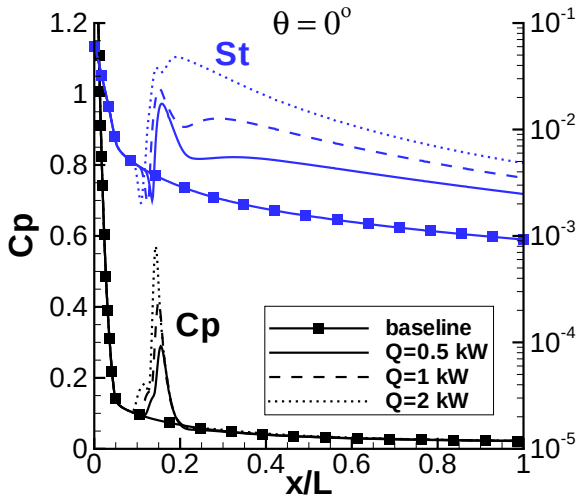

Figure 14. Pressure coefficient and Stanton number distributions along the top center line ($\theta = 0°$) of a Mach 14 blunt elliptic cone ($L = 0.2$ m) with various levels of energy deposition ($T_w = 294$ K).

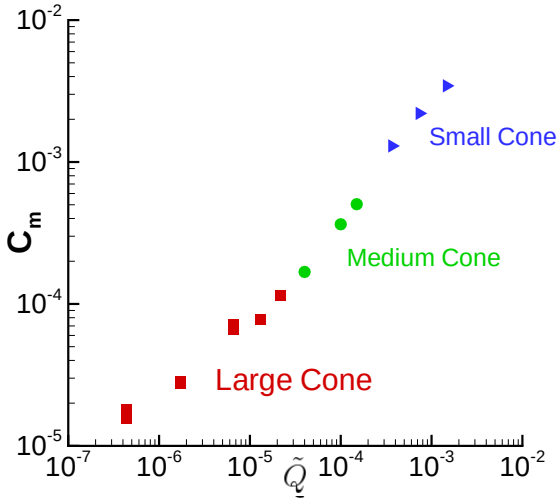

(a) Moment coefficient

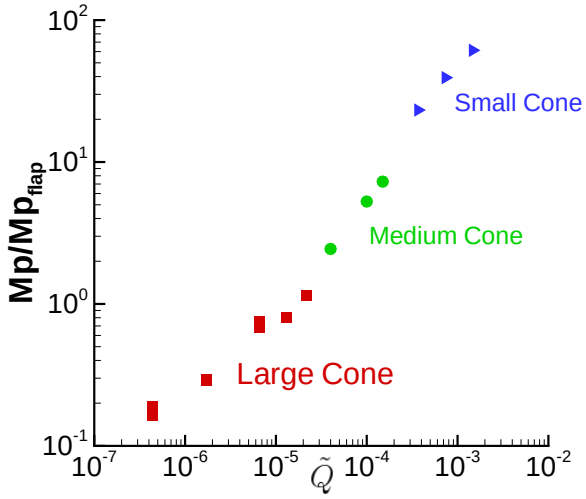

(b) Non-dimensional pitching moment

Figure 15. Moment coefficient and normalized change in pitching moment versus the nondimensional total power deposition $\tilde{Q}$ for various vehicle configurations (T_w = 300 K, thermal equilibrium, 5 sp., pancake deposition).